

# MOSFET Characteristics for Terahertz Detector Application From On-Wafer Measurement

Suna Kim, *Member, IEEE*, Dae-Woong Park, Kyoung-Young Choi, and Sang-Gug Lee, *Member, IEEE*

**Abstract**—In this paper, we report on MOSFET characteristics for terahertz (THz) detector application from precise on-wafer measurement, and the results are compared with theories and SPICE simulations. Techniques for precise measurement using a vector network analyzer and on-wafer probing and simulation based on the SPICE model are introduced. Several MOSFETs in various channel dimensions are fabricated in 65-nm CMOS technology and measured over gate bias voltage and the operating frequencies of 110, 200, and 300 GHz using the lock-in technique. The behavior of responsivity and noise equivalent power (NEP) depending on the channel width and length of the MOSFET and the frequency are investigated, and trends of the obtained results are in good agreement with the theories and the simulations. The channel width dependence of the responsivity of the MOSFET detector is evaluated and explained for the first time. The results of this work can provide a reliable and useful reference for the design of THz detectors.

**Index Terms**—Distributed resistive mixing, gate spreading resistance, loading effect, maximum oscillation frequency, MOSFET power detector, on-wafer measurement, parasitic gate to bulk capacitance, plasma wave detection, terahertz (THz) detection.

## I. INTRODUCTION

THE terahertz (THz) wave (submillimeter wave), which is located between electric waves and visible rays in the frequency spectrum, and thus has the features of both sides of the spectrum, can be used for a wide range of applications such as security, medical imaging, scientific imaging (biochemistry, chemistry, astronomy), manufacturing, and wireless communications. For imaging application in particular, THz detectors based on Schottky-barrier diodes, compound semiconductors, and strained- and bulk-silicon CMOS technologies have been a popular research topic for a number of years [1]–[8]. Among the various reported detectors, MOSFETs are emerging as a powerful candidate because of their frequency tunability by the gate bias voltage or the drain bias current and their relatively low noise at room temperature with fast response time, as well as low cost and a high degree of integration with other electronic circuitry.

Manuscript received November 06, 2014; revised April 28, 2015; August 12, 2015; September 24, 2015; accepted September 29, 2015. Date of publication October 26, 2015; date of current version November 23, 2015. This work was supported by the Pioneer Research Center Program through the National Research Foundation of Korea funded by the Ministry of Science, ICT & Future Planning under Grant 2012-0009594.

The authors are with Department of Electrical Engineering, Korea Advanced Institute of Science and Technology (KAIST), Daejeon 305-701, Korea (e-mail: suna.kim@kaist.ac.kr).

Digital Object Identifier 10.1109/TTHZ.2015.2487780

The operational principle of transistors near or beyond the cutoff frequency ( $f_T$ ), which is considered to be the highest operational frequency, can be explained by a physics-based plasma wave [9] or electronics-based distributed resistive mixing theories [10]. The plasma wave theory regards the channel of a transistor as a two dimensional (2D) electron gas as a whole that exhibits hydrodynamic behavior, and thus the generation of plasma waves in the channel by an external THz source can produce DC voltage or current in the channel. The distributed resistive mixing meanwhile regards the channel of a transistor as a non-quasi-static RC-ladder, such that each segment of the channel operates as a self-mixing power detector. Along with the mechanism for THz signal detection, the theories predict the detector characteristics as a function of the gate-to-channel voltage and have been extended to describe the channel dimension dependence. However, some works report conflicting results with each other with respect to the channel length dependence [7], [11], and moreover the channel width dependence of MOSFET detectors has not been reported to date.

With THz technologies, the measurement is also an issue due to the limitations of the measurement environment in terms of frequency, power, and accuracy. The frequency and power of THz technologies tend to be in a tradeoff relationship. As a signal source, electronic systems have limitations in generating high power at high frequencies, and photonic systems have the same limitations in a lower frequency regime [12], [13]. For these reasons, the THz signals, which are located at the upper edge of electronic waves and concurrently at the lower edge of photonic rays, are always hungry in terms of frequency and power. Systems for signal detection also suffer from the small power of the THz signal. Furthermore, a large amount of coupling and path losses make it difficult to conduct accurate experiments. Due to this accuracy limitation, many prior studies could not present absolute values of detector performances but instead show normalized figures in arbitrary units [3], [14]–[16].

In this paper, the responsivity and noise behavior of a MOSFET are analyzed in relation to channel dimension and frequency for THz detector application. In particular, the channel width dependence is evaluated for the first time. MOSFETs of various sizes are fabricated in 65-nm CMOS technology, and their performances are evaluated by precise on-wafer measurement for a number of frequencies. By using on-wafer  $S$ -parameter measurement, the reflected power at the input of the MOSFET, which is caused by the mismatch, can be calibrated out. Therefore, the responsivity of the detector in response to the transmitted power into the MOSFET can be obtained, and it corresponds to the maximum achievable responsivity for the given transistor sizes and frequencies. In this

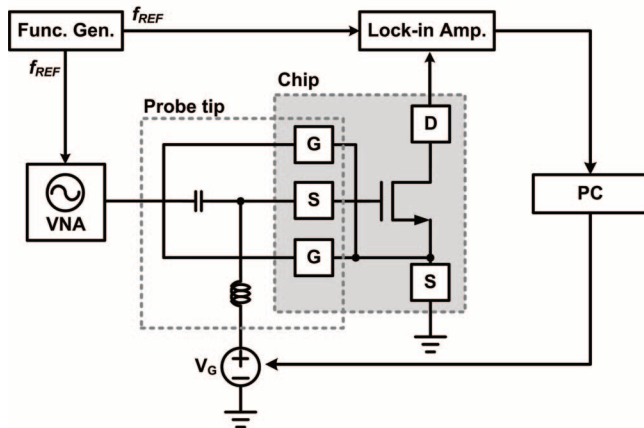


Fig. 1. Measurement setup for the MOSFET as a THz detector.

work, in addition to the reflection loss [17], [18], the insertion losses of the waveguide, probe, and pad are also compensated to achieve a more accurate estimation of the transmitted power into the input of the MOSFET. Auxiliary SPICE simulations are also performed for various channel dimensions and frequencies for comparison. Section II introduces the details of the measurement method using a vector network analyzer (VNA) and a simulation technique based on the SPICE model for the responsivity of the MOSFET. The dependence of the MOSFET responsivity as a function of channel width and length is presented in Section III. Section IV presents the frequency behavior of the responsivity, and Section V describes the noise equivalent power (NEP) versus the channel dimension. Lastly, a conclusion follows in Section VI.

## II. MEASUREMENT AND SIMULATION DETAILS

This section describes the measurement and simulation details of MOSFETs intended for use as THz detectors.

### A. Measurement Details

Fig. 1 shows the measurement setup for the detectors. An N-type MOSFET and GSG pads are laid-out for 1-port on-wafer measurement. A VNA is used for the THz signal source and dc gate bias is applied through the bias-T in the GSG probe tip. The THz signal is modulated by a 5-Hz trigger signal ( $f_{REF}$ ) provided by a function generator, and the output signal at the drain of the transistor is delivered into a 10-M $\Omega$  load, which is detected using a lock-in amplifier. A PC reads the output data from the lock-in amplifier for the given gate bias voltage, which is controlled by the PC.

Various sizes of n-MOSFETs are fabricated in a 65-nm CMOS technology. Fig. 2 shows a chip micrograph of one of the MOSFET detectors. The GSG pads for on-wafer probing are located at the left-hand side, and the pads connected to the drain (D) and source (S) terminals are for wire bonding. The MOSFET is located close to the GSG pad. The Metal-1 layer (the bottom layer of metal stack), which is connected to ground by the ground pads of GSG pads, is spread across the entire chip, and the source terminal of the MOSFET is connected to this Metal-1 and the source pad as well. The rest of the chip area and pads represents an integrated amplifier, which is not used

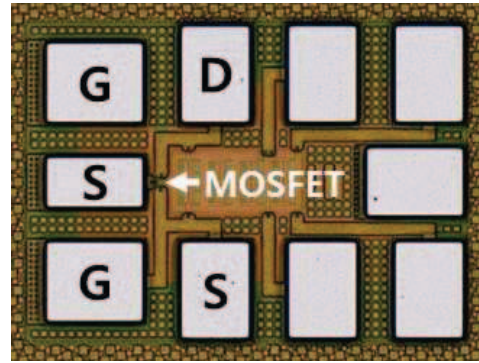
Fig. 2. Chip micrograph ( $386 \times 280 \mu\text{m}^2$ ).

TABLE I  
CHANNEL DIMENSIONS OF FABRICATED MOSFETs AND MEASURED FREQUENCY

	W	L	Measured frequency
1	$1 \mu\text{m} \times 4$	250 nm	300 GHz
2	$4 \mu\text{m} \times 1$	250 nm	300 GHz
3	$1 \mu\text{m} \times 1$	250 nm	300 GHz
4	$2 \mu\text{m} \times 1$	250 nm	300 GHz
5	$2 \mu\text{m} \times 1$	130 nm	110/200/300 GHz
6	$2 \mu\text{m} \times 1$	60 nm	300 GHz

in this work. Table I summarizes the channel dimensions of the fabricated MOSFETs and the measured frequency. Considering the theoretical analysis [8], [19] and experimental results [6], [7], the test patterns are designed mostly with 250 nm of channel length, which is the maximum length provided by 65-nm technology, for higher responsivity.

The voltage responsivity of THz detector is defined by

$$\text{Responsivity (V/W)} = \frac{\text{Output voltage (V)}}{\text{Input power (W)}}. \quad (1)$$

To characterize responsivity accurately for various sizes of transistors, the actual incident power into the transistor is estimated considering the measured values of the source power coming from the VNA, the loss from VNA to the transistor, and the reflection coefficient at the gate of transistor. Fig. 3 represents the small-signal equivalent circuit from the THz source ( $V_S$ ) to the input of the transistor ( $Z_L$ ). The source power coming from the VNA is measured with a power meter. Two 1-port calibrations, one at the output port of the VNA and the other at the probe tip, are performed, and then the macro function in the VNA can estimate the loss of the probe tip and waveguide. The reflection coefficient at the input pads ( $\Gamma_{in,pad}$ ) is obtained from the  $S$ -parameter measurement. The loss of the input pads and the interconnect line from the pad to the gate of transistor is estimated by an EM simulation. With the test structures shown in Fig. 2, the input pads as well as the interconnect line are shielded by Metal-1 ground layer, and thus the effect of the Si-substrate can be excluded in the measurement. Instead of lumped model-based (e.g., using open/short dummy structures) de-embedding, EM simulation based de-embedding is adopted. The latter is expected to be more accurate considering the high

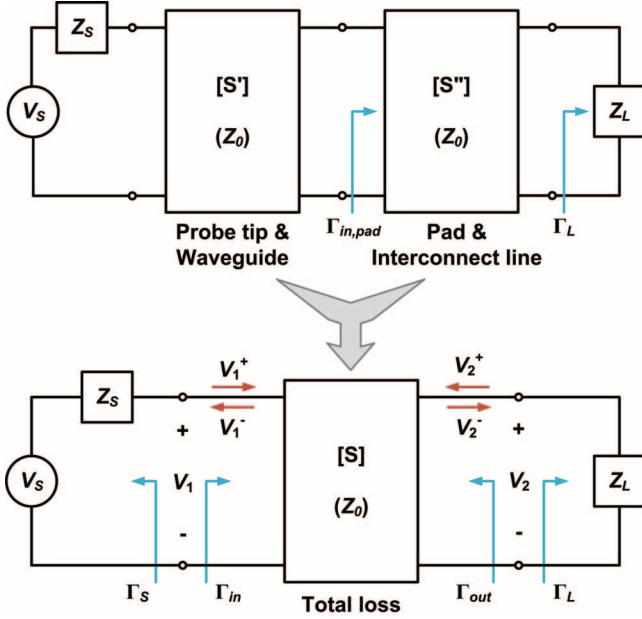


Fig. 3. Small-signal equivalent circuit from THz source to the input of the transistor.

operating frequencies and the simplified structure of the pads and interconnect line (metal-SiO<sub>2</sub>-metal). The reflection coefficient at the gate of transistor ( $\Gamma_L$ ) is estimated by the following relationship, which can be easily driven by the definition of the  $S$ -parameter

$$\Gamma_L = \frac{S''_{11} - \Gamma_{in,pad}}{\Delta'' - S''_{22}\Gamma_{in,pad}}, \quad (2)$$

where  $\Delta'' = S''_{11}S''_{22} - S''_{12}S''_{21}$  and  $S''_{xx}$  are the 2-port  $S$ -parameters of the pad and interconnect line. The characteristics of the probe tip and waveguide [ $S'$ ] and pad and interconnect line [ $S''$ ] can be merged in to a single 2-port network [ $S$ ] representing the total loss from the VNA to the transistor, as described in Fig. 3. The actual incident power into the gate-source terminal of the transistor  $P_L$  is given by

$$P_L = \frac{|S_{21}|^2(1 - |\Gamma_L|^2)}{|1 - S_{22}\Gamma_L|^2(1 - |\Gamma_{in}|^2)} P_{in} \quad (3)$$

where  $P_{in}$  is the source power,  $S_{xx}$  the 2-port  $S$ -parameters of the total loss, and  $\Gamma_{in}$  the input reflection coefficient, which is given by  $\Gamma_{in} = (S_{11} - \Delta\Gamma_L)/(1 - S_{22}\Gamma_L)$ , where  $\Delta = S_{11}S_{22} - S_{12}S_{21}$  [20]. The factor  $P_L/P_{in}$  in this work is  $-0.6 \sim -1.4$  dB,  $-0.2 \sim -0.4$  dB, and  $-0.07 \sim -0.2$  dB at 300, 200, and 110 GHz, respectively, depending on the gate bias voltage and channel dimension.

### B. Simulation Details

The MOSFET characteristics in terms of application as a THz detector are also investigated with a SPICE simulation. The commercially available SPICE model is not expected to predict the behaviors of MOSFETs with good accuracy at THz where the non-quasi-static effects are no longer negligible. Nevertheless, the simulation results based on the commercially available

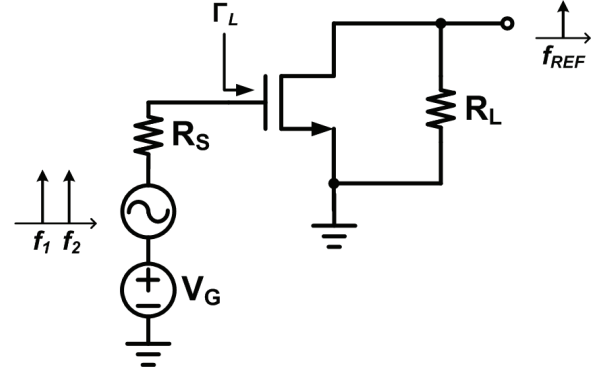


Fig. 4. Schematic of SPICE simulation for THz detectors.

MOSFET model show a good correlation with the measurement, as described later, making it useful for detector design from the perspective of providing guidelines.

Fig. 4 schematically illustrates the SPICE simulation setup for the THz signal detection where an n-MOSFET is excited by the THz signal at the gate and a load resistor ( $R_L$ ) detects the induced dc signal between the drain and source. To replicate the measurement setup, which adopts a lock-in amplifier, a two-tone signal is applied at the gate:  $f_1$  representing the THz signal and  $f_2$  the THz signal modulated by the reference signal,  $f_{REF}$  ( $f_2 = f_1 + f_{REF}$ ). Along with the two-tone signal, a DC bias voltage  $V_G$  is applied at the gate while no DC bias is applied at the drain terminal. For the given two-tone signal, the voltage magnitude of  $f_{REF}$  at the drain is read as an output response. The responses are simulated for various channel dimensions of n-MOSFETs over different frequencies. Because the responsivity is a function of the power delivered to the input,  $S$ -parameter simulations are also carried out at  $f_1$  to consider the return loss ( $\Gamma_L$ ) for all devices in Table I. Fig. 5 shows the measured  $\Gamma_{in,pad}$ , measured  $\Gamma_L$ , and simulated  $\Gamma_L$  ( $\Gamma_{L,sim}$ ) versus frequency for a  $W/L = 1 \mu\text{m} \times 4/250 \text{ nm}$  MOSFET. There is a significant gap between the measured and simulated  $\Gamma_L$ , but they are similar in terms of frequency behavior. The behaviors of  $\Gamma_L$ , measured and simulated, over the variations in the MOSFET dimensions ( $W/L$ ) also show similar trends (this is not shown in Fig. 5). As we do not expect accurate results from the simulation, all of the simulation results are plotted after normalization to depict relative behaviors only.

## III. RESPONSIVITY VERSUS CHANNEL DIMENSION OF MOSFETS

Here, the measured responsivity of MOSFET detectors for various channel dimensions are described in comparison with theory and SPICE simulations.

### A. Channel Width Dependence

In the plasma wave theory, the responsivity degradation of MOSFETs with an increase in channel width is explained by the oblique plasma wave propagation to the direction of the width [21]. However, this explanation is applicable only to the case of resonant mode plasma wave operation where the plasma wave travels back and forth between the source and drain terminals. In the non-resonant mode operation as in the case of MOSFET

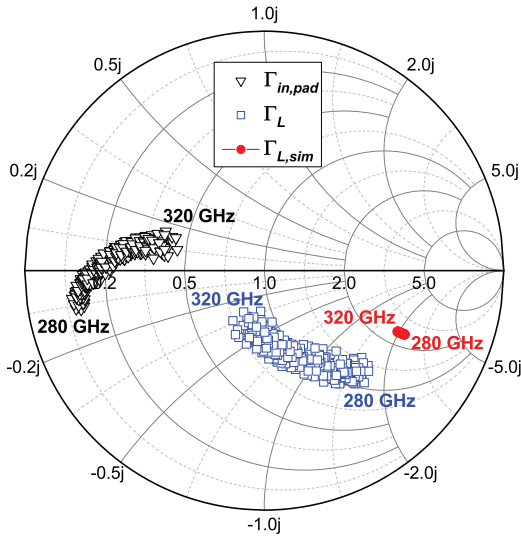


Fig. 5. Measured  $\Gamma_{in,pad}$ , measured  $\Gamma_L$ , and simulated  $\Gamma_L$  versus frequency for  $W/L = 1 \mu\text{m} \times 4/250 \text{ nm}$  MOSFET.

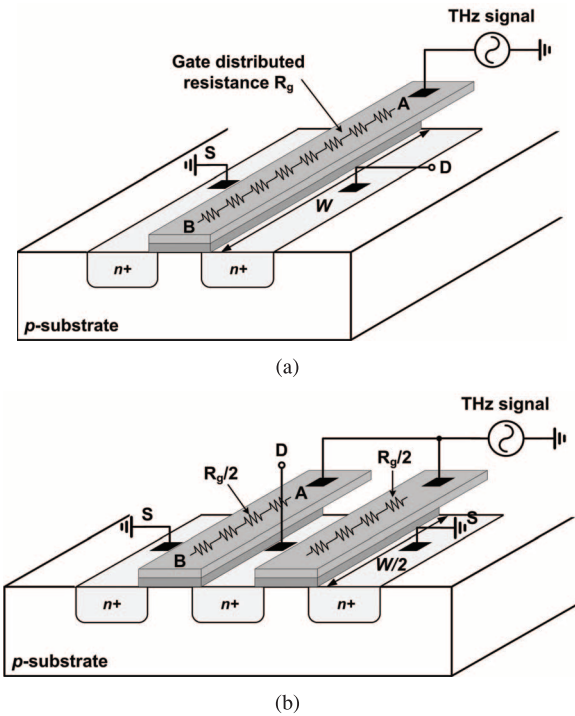


Fig. 6. Two MOSFET structures with different unit channel width.

detectors, the dependence of responsivity on the channel width has not been understood well. In the present work, this will be firstly explained by the high-frequency transit mode operation of MOSFETs.

Fig. 6 shows two MOSFET structures with the same total width but different finger width. In Fig. 6(a), due to the poly-silicon gate spreading resistance  $R_g$ , the THz signal applied at point A is the strongest and diminishes toward point B. Accordingly, the DC response induced between the drain and the source is smallest at point B. However, when the same channel width of the transistor is divided into two fingers, as in Fig. 6(b), the gate spreading resistance between points A and B becomes

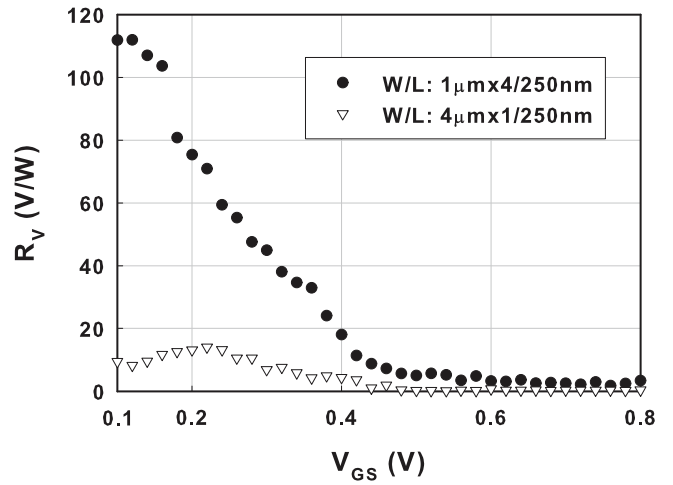


Fig. 7. Measured responsivity versus  $V_{GS}$  at 300 GHz for two different finger widths.

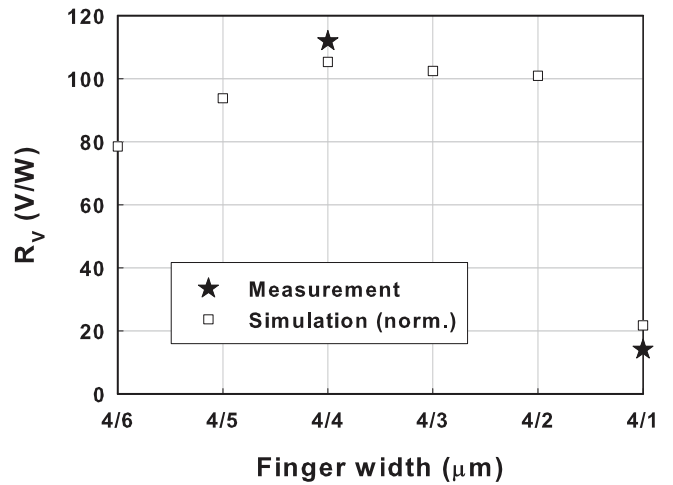


Fig. 8. Measured and simulated responsivity at 300 GHz for  $W/L = 4 \mu\text{m}/250 \text{ nm}$  MOSFET as a function of finger width.

$R_g/2$  while the variations in other small-signal parameters are negligible [22]. Consequently, the attenuation of the THz signal at point B is less severe, and hence the induced dc response between the drain and the source becomes larger.

Fig. 7 shows the measured responsivity ( $R_V$ ) versus gate-to-source voltage ( $V_{GS}$ ) at 300 GHz for  $W/L = 1 \mu\text{m} \times 4/250 \text{ nm}$  and  $W/L = 4 \mu\text{m} \times 1/250 \text{ nm}$  MOSFET. In Fig. 7, the device with finger width of  $1 \mu\text{m}$  shows more than five times higher responsivity than that of the  $4 \mu\text{m}$  case.

The simulated responsivity at 300 GHz as a function of finger width (total width/number of fingers) is shown in Fig. 8 after normalization while keeping the overall channel width and channel length fixed at  $4 \mu\text{m}$  and  $250 \text{ nm}$ , respectively. In Fig. 8, the responsivity at each finger width represents the maximum  $R_V$  that is obtained over the variation of  $V_{GS}$ . The measured results shown in Fig. 8 are the maximum value of devices shown in Fig. 7. In the simulation results, for the cases from 1- to 4-finger transistors, an increase in the number of fingers, i.e., a decrease in the finger width, leads to higher responsivity, as observed in the measured results. The higher responsivity with a decrease in finger width can be explained

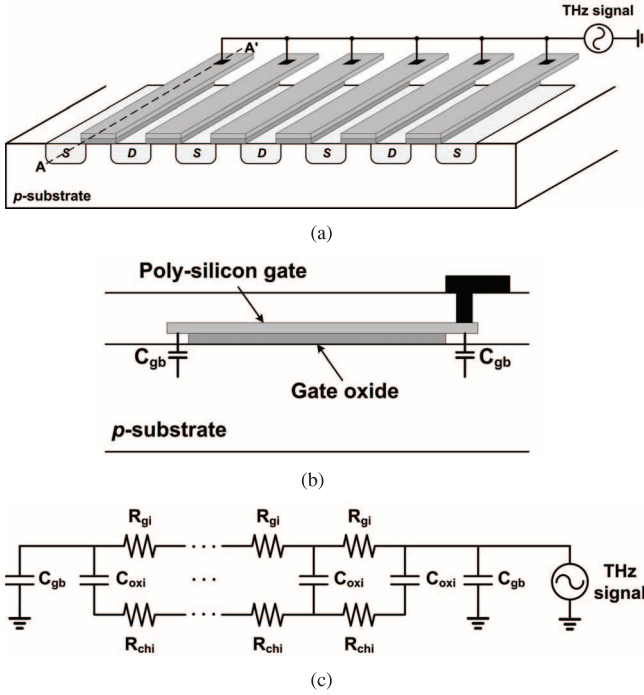


Fig. 9. Multifinger MOSFET. (a) Structure. (b) A-A' cross section. (c) Small-signal equivalent circuit.

by the decrease in poly-silicon gate spreading resistance,  $R_g$ . However, the simulated responsivity of the 5- and 6-finger transistors tends to decrease again. This can be explained using Fig. 9.

Fig. 9(a) shows the structure of a multifinger MOSFET. The cross section of the dashed line along points A and A' is shown in Fig. 9(b), where  $C_{gb}$  represents the parasitic overlap capacitance between the gate and body terminals. According to the [23],  $C_{gb} = 0.08$  fF for a unit finger of transistor with  $L = 65$  nm, and as the number of fingers increases, the total  $C_{gb}$  increases proportionally. Therefore, in the equivalent circuit shown in Fig. 9(c), with an increase in the number of fingers, even though the value of  $R_g$  decreases,  $C_{gb}$  becomes a large portion of the total oxide capacitance, and consequently the voltage along the channel width decreases by the shunting effect of  $C_{gb}$  [24], leading to responsivity degradation.

The characteristics of responsivity depending on  $R_g$  and  $C_{gb}$  resemble those of maximum oscillation frequency  $f_{max}$ , which is the frequency where the maximum available power gain of the transistor becomes one, given by

$$f_{max} = \frac{f_T}{2\sqrt{2\pi f_T R_g C_{gd} + g_{ds} R_{in}}} \quad (4)$$

where  $C_{gd}$  is the parasitic gate-drain capacitance,  $g_{ds}$  the channel conductance,  $R_{in}$  the real part of the input impedance, and  $f_T$  the cutoff frequency, which is given by

$$f_T = \frac{g_m}{2\pi(C_{gs} + C_{gd})} \quad (5)$$

where  $g_m$  is the transconductance and  $C_{gs}$  the parasitic gate-source capacitance. Equation (4) shows that an increase in  $R_g$  directly leads to a decrease in  $f_{max}$ . When the source

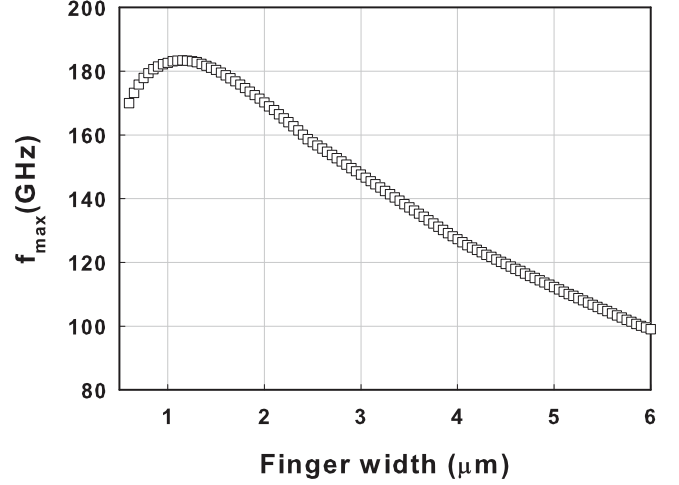


Fig. 10. Simulated  $f_{max}$  as a function of finger width.

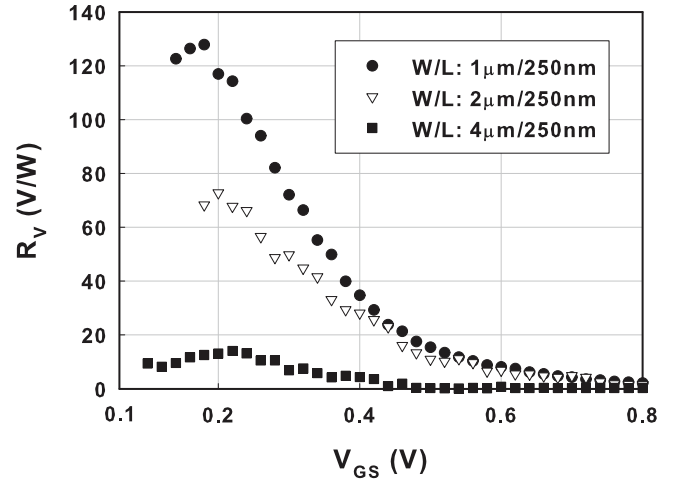


Fig. 11. Measured responsivity versus  $V_{GS}$  at 300 GHz for three different channel widths.

and body terminals are tied together,  $C_{gb}$  becomes a capacitance connected in parallel with  $C_{gs}$ . When  $C_{gb}$  becomes significant in multi-finger transistors (for a single finger of  $W/L = 2 \mu\text{m}/65$  nm MOSFET,  $C_{gb} \approx C_{gs}/14$  [23]), the cutoff frequency should be represented as

$$f_T = \frac{g_m}{2\pi(C_{gs} + C_{gb} + C_{gd})} \quad (6)$$

which leads to  $f_T$  and hence  $f_{max}$  degradation. Fig. 10 shows the simulated  $f_{max}$  as a function of finger width while  $L = 60$  nm,  $V_G = 500$  mV, and  $V_D = 1$  V.  $f_{max}$  plotted in Fig. 10 shows a similar dependence on finger width as the responsivity in Fig. 8.

Fig. 10 shows that large channel width is associated with lower  $f_{max}$  for single-finger transistors. The measured responsivity of single-finger transistors with three different channel widths reveals a similar trend to  $f_{max}$  as plotted in Fig. 11. In this case,  $C_{gs}$  also has a partial contribution to the responsivity like  $C_{gb}$ , shunting the input of transistor. The responsivity at 300 GHz as a function of the MOSFET channel width while keeping  $L = 250$  nm is simulated and shown in Fig. 12 after normalization along with the measured responsivities of three

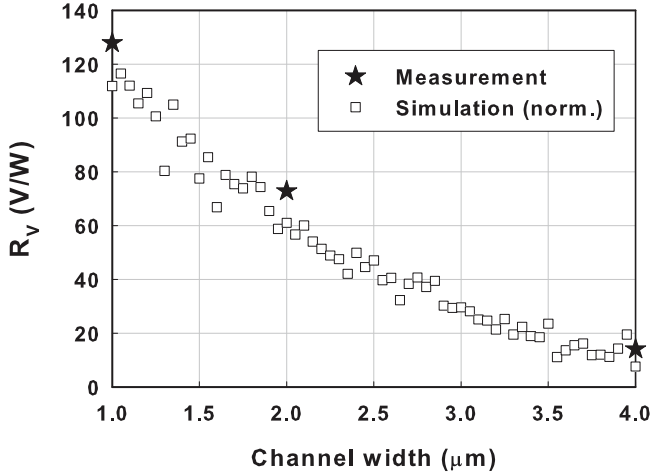


Fig. 12. Measured and simulated responsivity at 300 GHz as a function of MOSFET channel widths.

devices. The measured results in Fig. 12 are the maximum value of each device shown in Fig. 11. The decreasing trend in simulated responsivity with an increase in channel width agrees with the measurement results.

### B. Channel Length Dependence

Based on the plasma wave theory, the plasma wave decays well before the end of the channel if the length of the channel is much longer than the characteristic length of decay  $L_0$ , given by [16]

$$L_0 = \sqrt{\frac{\mu n}{\omega (dn/dU) |_{U=U_{gt}}} \quad (7)$$

where

$$n(U) = \frac{C\eta k_B T}{e^2} \ln \left[ 1 + \exp \left( \frac{eU}{\eta k_B T} \right) \right] \quad (8)$$

where  $\mu$  is mobility,  $C$  is the gate-to-channel capacitance per unit area,  $k_B$  is the Boltzmann constant,  $T$  is temperature,  $e$  is the electron charge,  $\eta$  is the subthreshold ideality factor, and  $U$  is the gate-to-channel voltage swing, given by  $U = U_{gt} - U_{ch}$ , where  $U_{gt} = U_g - U_t$  is the gate voltage swing,  $U_g$  and  $U_t$  the gate and threshold voltages, respectively, and  $U_{ch}$  is the channel voltage. For the given 65-nm technology, using the typical values of  $\mu = 157 \text{ cm}^2/\text{Vs}$ ,  $C = 0.019 \text{ F/m}^2$ ,  $T = 300 \text{ K}$ ,  $\eta = 1.45$  [16], and  $U = 0 \text{ V}$ ,  $L_0$  of devices in this work at 300 GHz is expected to be about 21 nm. In this case, the transistor acts as a broadband (nonresonant) detector.

In the principle of distributed resistive mixing, the THz signal is rectified at each segment of the distributed channel, producing a dc voltage drop along the channel [10]. Both plasma wave theory and distributed resistive mixing principle predict a dc voltage drop along the channel with decreasing amplitude in each segment toward the drain terminal. Following these principles, because the resulting drain–source voltage is given by the integrated sum of the voltage drop along the channel, a longer channel is expected to produce a higher dc response.

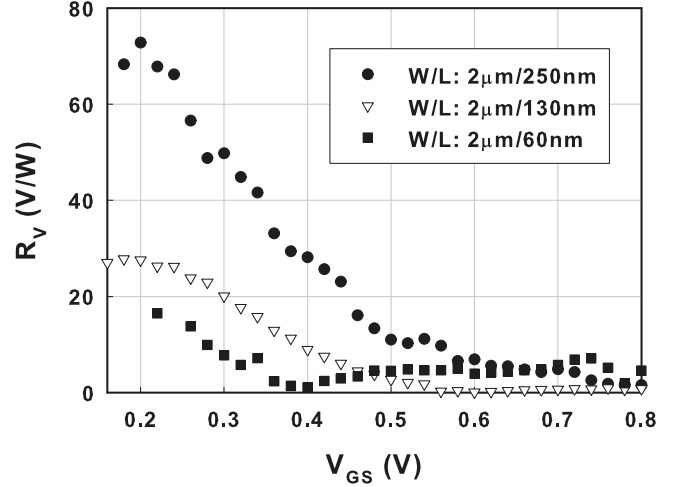


Fig. 13. Measured responsivity versus  $V_{GS}$  at 300 GHz for three different channel lengths.

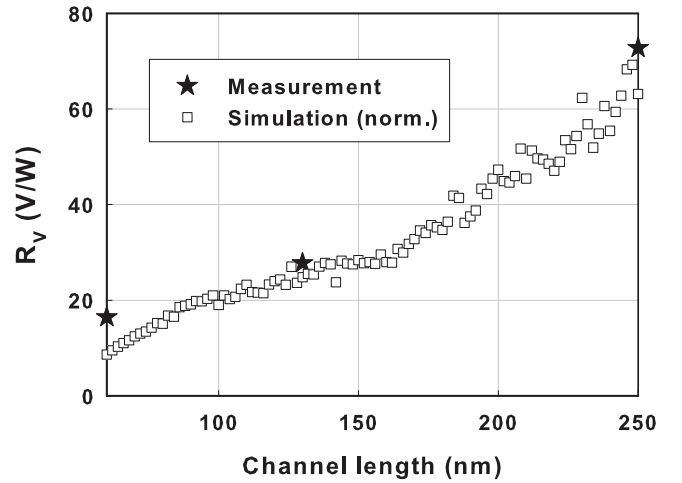


Fig. 14. Measured and simulated responsivity at 300 GHz as a function of MOSFET channel length.

Fig. 13 shows the measured responsivity versus  $V_{GS}$  at 300 GHz for three different channel lengths. As predicted by the theories, long channel devices show higher responsivity.

The simulated responsivity at 300 GHz as a function of channel length is shown in Fig. 14 after normalization along with the measured responsivities of the three devices shown in Fig. 13. The measurement results shown in Fig. 14 are the maximum responsivity of each device in Fig. 13. Both the simulated and the measured responsivity increase with an increase in the channel length. In the two theories, however, the responsivity is expected to saturate for the device of  $L = 130 \text{ nm}$ , because at this dimension the plasma wave oscillation is expected to decrease down to  $e^{-(130/21)} \approx 0.2\%$  of the initial value. This discrepancy can be attributed to the decrease in  $R_g$ ; at the same position of the channel, the amplitude of the THz signal of the  $L = 250\text{-nm}$  device becomes stronger than that of the  $L = 130\text{-nm}$  device because of the lower value of  $R_g$ .

However, [11] reported contradictory dependence on channel length such that devices with shorter channel length showed higher responsivity. This controversy can be explained by

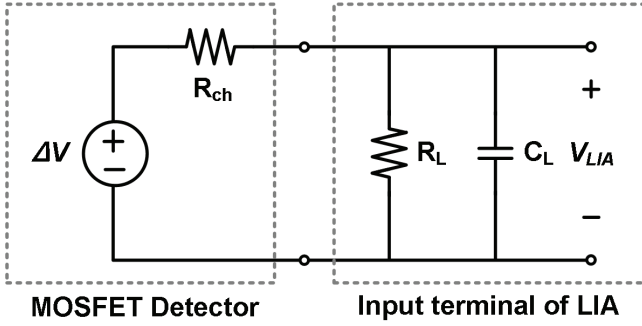


Fig. 15. Equivalent circuit of MOSFET detector and input terminal of LIA to show loading effect between them.

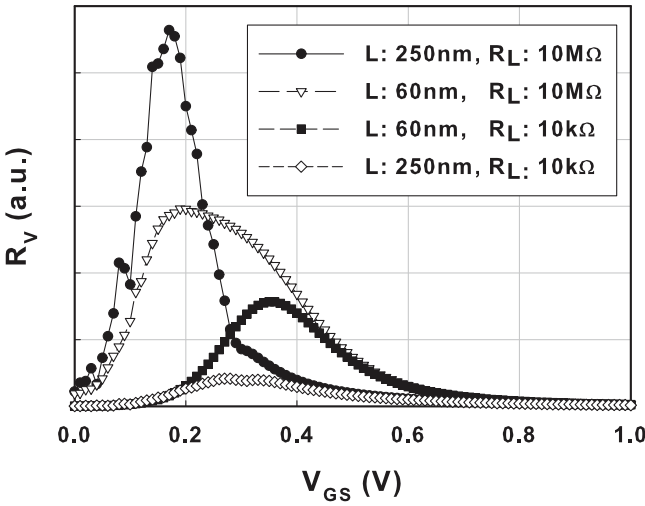


Fig. 16. Simulated responsivity versus  $V_{GS}$  at 300 GHz for  $L = 60/250$ -nm transistors with  $R_L = 10 \text{ M}\Omega/10 \text{ k}\Omega$ .

the loading effect. Fig. 15 shows the equivalent circuit of the MOSFET detector and input impedance of the lock-in amplifier (LIA) to explain the loading effect on the MOSFET detector. In Fig. 15, the voltage response of the MOSFET detector ( $\Delta V$ ) drops across the channel resistance ( $R_{ch}$ ) and load impedance ( $Z_L = R_L \parallel 1/j\omega_{REF}C_L$ ). The output voltage delivered to LIA ( $V_{LIA}$ ) is given by

$$V_{LIA} = \frac{\Delta V}{1 + R_{ch}/Z_L} \quad (9)$$

by the voltage division rule. By the loading effect, depending on the value of the ratio  $R_{ch}/Z_L$ ,  $V_{LIA}$  is not always proportional to  $\Delta V$ . Fig. 16 shows the simulated responsivity versus  $V_{GS}$  at 300 GHz for the MOSFETs with channel length of 60 and 250 nm with load resistance  $R_L$  of 10 M $\Omega$  and 10 k $\Omega$ , respectively. In Fig. 16, longer channel device shows higher responsivity with  $R_L = 10 \text{ M}\Omega$ . In contrast, with  $R_L = 10 \text{ k}\Omega$ , shorter channel device shows higher responsivity due to the loading effect. The modulation frequency ( $f_{REF}$ ) described in Section II can also affect on  $V_{LIA}$  because  $Z_L$  is a function of  $\omega_{REF}$ , but with the measurement reported in this work, it is negligible because  $f_{REF}$  is only 5 Hz.

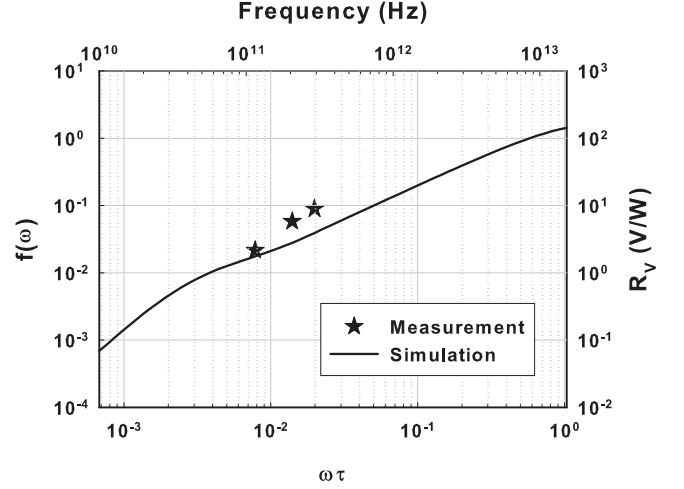


Fig. 17. Numerically simulated and measured responsivity versus  $\omega\tau$  and the frequency, respectively.

#### IV. RESPONSIVITY VERSUS FREQUENCY

In the plasma wave theory, the responsivity of an FET is proportional to the following function [19]:

$$f(\omega) = 1 + \beta - \frac{1 + \beta \cos(2k'_o L)}{\sinh^2(k''_o L) + \cos^2(k'_o L)} \quad (10)$$

where

$$\beta = \frac{2\omega\tau}{\sqrt{1 + (\omega\tau)^2}} \quad (11)$$

$$k'_o = \frac{\omega}{s} \left( \frac{(1 + \omega^{-2}\tau^{-2})^{1/2} + 1}{2} \right)^{1/2}$$

$$k''_o = \frac{\omega}{s} \left( \frac{(1 + \omega^{-2}\tau^{-2})^{1/2} - 1}{2} \right)^{1/2} \quad (12)$$

where  $L$  is the channel length,  $\omega$  the angular frequency,  $\tau$  the electron momentum relaxation time, and  $s$  the wave velocity. In a 65-nm CMOS technology,  $\tau = \mu m^*/e$  at room temperature is about 0.01 ps, where  $\mu$  is the electron mobility,  $m^*$  the electron effective mass, and  $e$  the electron charge. Fig. 17 depicts the function  $f(\omega)$  versus  $\omega\tau$  as a solid line for the case of  $\tau = 0.01$  ps and  $L = 130$  nm. The corresponding operational frequency to  $\omega\tau$  is indicated at the top  $x$ -axis in Fig. 17. In Fig. 17, where  $\omega\tau \ll 1$ , the responsivity increases with frequency almost dB-linearly. In resonant mode plasma wave detectors, resonances by plasma wave oscillation can occur where  $\omega\tau \gg 1$ , but in nonresonant mode plasma wave detectors such as in the case of conventional MOSFETs, the plasma wave oscillation is overdamped [19]. In the distributed resistive mixing model, higher responsivity with an increase in frequency can be explained by the reduction in the impedance of  $C_{gd}$ , which leads to a higher voltage swing at the drain node, and hence additional dc voltage is induced in the channel.

In Fig. 18, the measured responsivity for the input frequencies of 110, 200, and 300 GHz are plotted for a MOSFET of  $W/L = 2 \text{ }\mu\text{m}/130 \text{ nm}$  with  $V_{GS} = 0.4$  V. The measurement results follow the increasing trend of  $f(\omega)$ . Fig. 18 shows the measured responsivity of the same device as a function of  $V_{GS}$

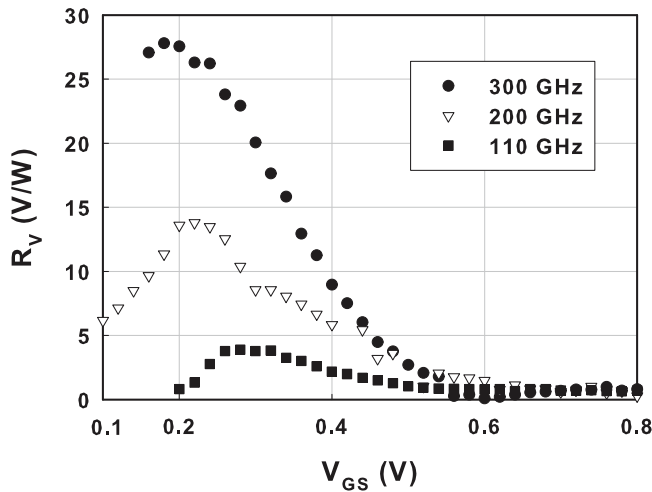


Fig. 18. Measured responsivity of  $W/L = 2 \mu\text{m}/130 \text{ nm}$  MOSFET versus  $V_{GS}$  at three different frequencies.

at three different frequencies, and the increase in responsivity with frequency is well demonstrated.

#### V. NOISE EQUIVALENT POWER

Heretofore, the responsivity characteristics of the MOSFET are investigated in terms of the channel dimension and frequency dependencies. However, the more important metric for a THz detector is the noise equivalent power (NEP), which is given by

$$\text{NEP} (W/\sqrt{\text{Hz}}) = \frac{\text{Noise spectral density} (V/\sqrt{\text{Hz}})}{\text{Responsivity} (V/W)}. \quad (13)$$

Because MOSFET detectors are used under an open-drain condition, that is,  $I_D = 0$ , the  $1/f$  noise is not an issue; the only noise consideration is the channel thermal noise, which is given by  $\sqrt{N} = \sqrt{4kTR_{ch}}$ , where  $k$  is the Boltzmann constant,  $T$  the absolute temperature, and  $R_{ch}$  the channel resistance. From the dc measurement of the channel resistance, the thermal noise of each MOSFET at a given  $V_{GS}$  can be estimated.

The NEP is a more important metric for a THz detector than the responsivity, because it determines the signal-to-noise ratio of a detection system. The design guidelines to achieve higher responsivity are discussed in Section III, and to achieve a low NEP, the noise spectral density (NSD) should be minimized. Because of the dependence on  $R_{ch}$ , the NSD can be reduced by increasing the  $W/L$  ratio of the channel. Fig. 19 shows the measured NEP at 300 GHz versus  $V_{GS}$  for three different channel widths while keeping  $L = 250 \text{ nm}$ . Although the NSD is inversely proportional to  $\sqrt{W}$  (7.0, 10.0, and 14.5  $\text{nV}/\sqrt{\text{Hz}}$  at  $V_{GS} = 0.3 \text{ V}$  for  $W = 4, 2, 1 \mu\text{m}$ , respectively), the MOSFET with of  $W/L = 4 \mu\text{m}/250 \text{ nm}$  shows the highest NEP due to the poorest responsivity. The NEP values of the other two devices are comparable because of the opposite behavior of the responsivities and NSDs depending on the channel width.

From Fig. 19, the responsivity should be improved to achieve a lower NEP while keeping the NSD low, and Fig. 20 gives the solution. Fig. 20 shows the dependence of the measured NEP

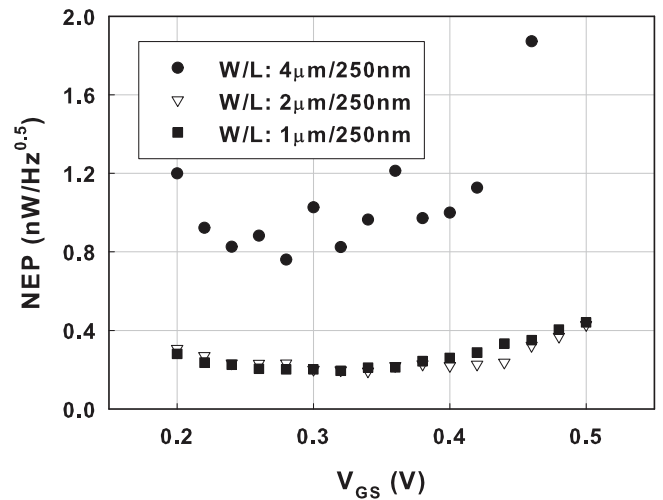


Fig. 19. Measured NEP at 300 GHz versus  $V_{GS}$  for three different channel widths.

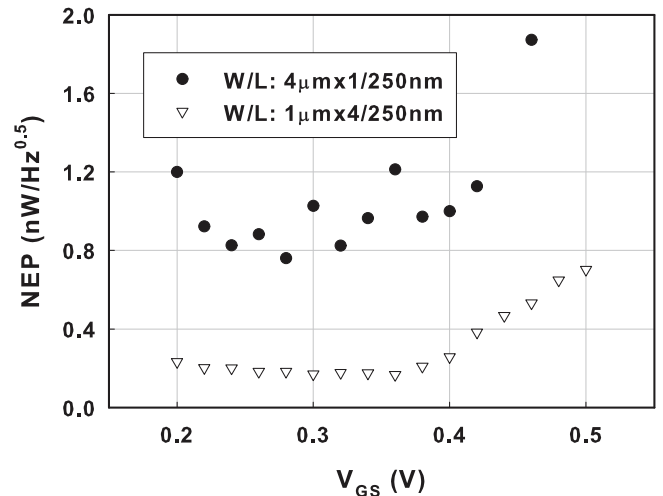


Fig. 20. Measured NEP at 300 GHz versus  $V_{GS}$  for two different finger widths.

at 300 GHz on the finger width as a function of  $V_{GS}$ . Because the NSD values of the two devices are identical due to the same overall  $W/L$  ratio, the behavior of the NEP is determined by the responsivity (6.9 and 44.9  $\text{V}/W$  for  $W = 4 \mu\text{m} \times 1$  and  $1 \mu\text{m} \times 4$ , respectively, at  $V_{GS} = 0.3 \text{ V}$ ). The NEP is improved from 0.76 to 0.18  $\text{nW}/\sqrt{\text{Hz}}$  at  $V_{GS} = 0.28 \text{ V}$  due to the higher responsivity by reducing the finger width.

Fig. 21 compares the NEP values of two MOSFETs with the same finger width but different number of fingers,  $W/L = 1 \mu\text{m} \times 4/250 \text{ nm}$  and  $1 \mu\text{m} \times 1/250 \text{ nm}$ . Although the two MOSFETs have the same finger width, the device with a single-finger transistor showed higher responsivity (by comparing Figs. 7 and 11) because of fewer parasitic components such as overlap capacitance and spreading resistance from interconnect lines. In Fig. 21, however, near the minimum point of the NEP, the lower NSD of the  $W/L = 1 \mu\text{m} \times 4/250 \text{ nm}$  transistor provides a greater contribution to reducing NEP than the higher responsivity of the  $W/L = 1 \mu\text{m} \times 1/250 \text{ nm}$  transistor. Considering that the NEP represents overall performance of the THz detector, the channel dimensions of the MOSFET detector

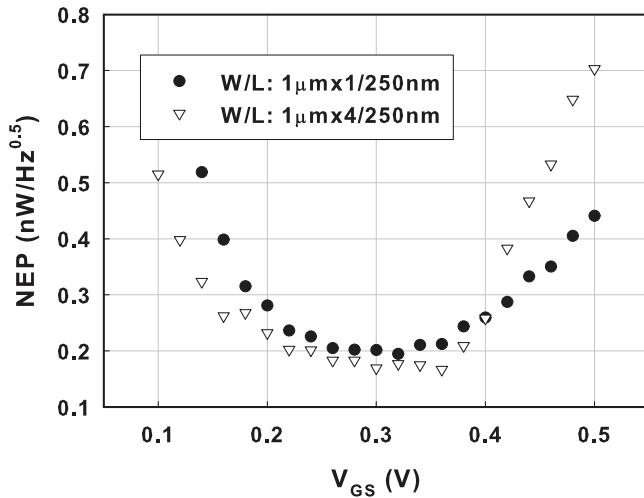


Fig. 21. Measured NEP at 300 GHz versus  $V_{GS}$  for two different transistors.

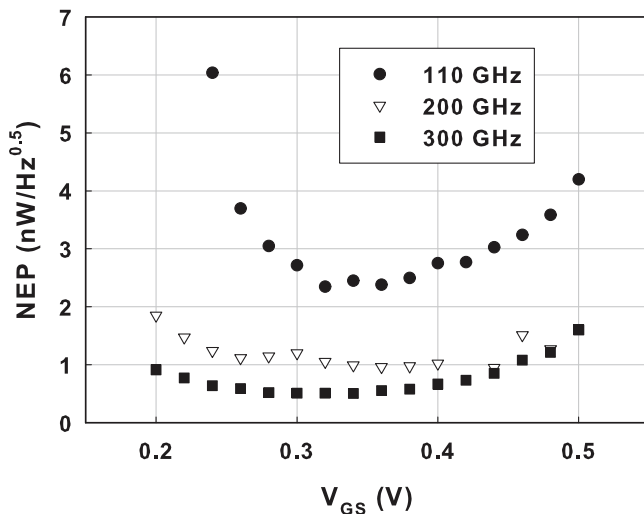


Fig. 22. Measured NEP of  $W/L = 2 \mu\text{m}/130 \text{ nm}$  MOSFET versus  $V_{GS}$  at three different frequencies.

should be decided carefully by keeping the NSD low with a wide channel and the responsivity high with short finger width.

Fig. 22 shows the measured NEP of  $W/L = 2 \mu\text{m}/130 \text{ nm}$  MOSFET versus  $V_{GS}$  at three different frequencies. Higher responsivity (among 3.9, 13.8, and 27.8 V/W at 100, 200, and 300 GHz, respectively, when  $V_{GS} = 0.3 \text{ V}$ ) directly leads to a lower NEP because NSDs are identical ( $9.5 \text{ nV}/\sqrt{\text{Hz}}$  at  $V_{GS} = 0.3 \text{ V}$ ). From Fig. 22, increasing operating frequency can also be a good solution for performance enhancement of a THz detector.

## VI. CONCLUSION

The characteristics of MOSFET in terms of application as a THz detector are reported from precise on-wafer measurements and the results are compared to theories and simulations. The techniques for precise measurement using a VNA and on-wafer probing and a simulation based on the SPICE model are introduced. Several MOSFETs in various channel dimensions are fabricated in 65-nm CMOS technology and measured over  $V_{GS}$  and operating frequencies of 110, 200, and 300 GHz using the lock-in technique. The behavior of the responsivity and the NEP

depending on the channel width and length of the MOSFET and the frequency are investigated, and the observed trends are in good agreement with the theories and the simulations.

The channel width dependence of the responsivity for a non-resonant MOSFET detector is evaluated and explained for the first time. The responsivity degradation with an increase in finger width is explained by the THz signal loss along the spreading resistance of the poly-silicon gate fingers. Considering noise characteristics as well, wide channel device in a multi-finger layout is recommended for higher responsivity and lower NEP unless the parasitic  $C_{gb}$  becomes significant. The controversy of the channel length dependence on responsivity is also resolved in this work by considering the loading effect on the MOSFET detector.

Compared to the measurement results of free space radiation, those of on-wafer probing are more accurate in that the exact amount of power transmitted into the MOSFET could be obtained by calibrating out the insertion/reflection losses of the cables, probe, pads, interconnect line, and the impedance at the gate of the transistor. Thus, the responsivities presented in this work are the maximum achievable values for the given technology, transistor size, and frequency. In applications to the free space environment, the results of this work can provide a reliable and useful reference for selecting the optimum transistor dimensions and the maximum achievable responsivity under perfect matching (conjugate matching) between the antenna and the corresponding MOSFET detector.

## ACKNOWLEDGMENT

The authors would like to thank Dr. J.-S. Kang at Korea Research Institute of Standards and Science (KRISS) for his support in carrying out the measurements.

## REFERENCES

- [1] R. Han, Y. Zhang, Y. Kim, D. Y. Kim, H. Shichijo, E. Afshari, and O. Kenneth, "280 GHz and 860 GHz image sensors using Schottky-barrier diodes in  $0.13 \mu\text{m}$  digital CMOS," in *Proc. IEEE ISSCC*, San Francisco, CA, USA, 2012, pp. 254–256.
- [2] S. P. Han, H. Ko, J. W. Park, N. Kim, Y. J. Yoon, J. H. Shin, D. Y. Kim, D. H. Lee, and K. H. Park, "InGaAs Schottky barrier diode array detector for a real-time compact terahertz line scanner," *Opt. Exp.*, vol. 21, no. 22, pp. 25874–25882, Nov. 2013.
- [3] S. Boubanga-Tombet, F. Tepe, D. Coquillat, S. Nadar, N. Dyakonova, H. Videlier, W. Knap, A. Shechetov, C. Gardès, Y. Roelens, S. Bol-laert, D. Seliuta, R. Vadoklis, and G. Valušis, "Current driven resonant plasma wave detection of terahertz radiation: Toward the Dyakonov-Shur instability," *Appl. Phys. Lett.*, vol. 92, no. 21, May 2008, Art. ID 212101.
- [4] M. S. Shur and J. Q. Lü, "Terahertz source and detectors using two-dimensional electronic fluid in high electron-mobility transistors," *IEEE Trans. Microw. Theory Techn.*, vol. 48, no. 4, pp. 750–756, Apr. 2000.
- [5] S. L. Rumyantsev, K. Fobelets, D. Veksler, T. Hackbarth, and M. S. Shur, "Strained-Si modulation doped field effect transistors as detectors of terahertz and sub-terahertz radiation," *Semicond. Sci. and Technol.*, vol. 23, no. 10, pp. 105001-1–105001-4, Oct. 2008.
- [6] H. Videlier, S. Nadar, N. Dyakonova, M. Sakowicz, T. T. V. Dam, F. Tepe, D. Coquillat, W. Knap, S. Denorme, T. Skotnicki, J. M. Peiris, and J. Lyonnet, "Silicon MOSFET as room temperature terahertz detectors," in *J. Phys.: Conf. Series*, Aug. 2009, vol. 193, no. 1, pp. 012095-1–012095-4.
- [7] R. Tauk, F. Tepe, S. Boubanga, D. Coquillat, W. Knap, Y. M. Meziani, C. Gallon, F. Boeuf, T. Skotnicki, C. Fenouillet-Beranger, D. K. Maude, S. Rumyantsev, and M. S. Shur, "Plasma wave detection of terahertz radiation by silicon field effect transistors: Responsivity and noise equivalent power," *Appl. Phys. Lett.*, vol. 89, no. 25, Dec. 2006, Art. ID 253511.

- [8] A. Lissauskas, U. Pfeiffer, E. Öjefors, P. H. Bolivar, D. Glaab, and H. G. Roskos, "Rational design of high-responsivity detectors of terahertz radiation based on distributed self-mixing in silicon field-effect transistors," *J. Appl. Phys.*, vol. 105, no. 11, Jun. 2009, Art. ID 114511.
- [9] M. Dyakonov and M. Shur, "Shallow water analogy for a ballistic field effect transistor: New mechanism of plasma wave generation by dc current," *Phys. Rev. Lett.*, vol. 71, no. 15, pp. 2465–2468, Oct. 1993.
- [10] E. Öjefors, U. R. Pfeiffer, A. Lissauskas, and H. G. Roskos, "A 0.65 THz focal-plane array in a quarter-micron CMOS process technology," *IEEE J. Solid-State Circuits*, vol. 44, no. 7, pp. 1968–1976, Jul. 2009.
- [11] W. Stillman, F. Guarin, V. Y. Kachorovskii, N. Pala, S. Rumyantsev, M. S. Shur, and D. Veksler, "Nanometer scale complementary silicon MOSFETs as detectors of terahertz and sub-terahertz radiation," in *Proc. IEEE Sensors Conf.*, Atlanta, GA, USA, 2007, pp. 934–937.
- [12] P. H. Siegel, "Terahertz technology," *IEEE Trans. Microw. Theory Techn.*, vol. 50, no. 3, pp. 910–928, Mar. 2002.
- [13] D. J. Paul, "The progress towards terahertz quantum cascade lasers on silicon substrates," *Laser Photon. Rev.*, vol. 4, no. 5, pp. 610–632, June 2010.
- [14] W. Stillman, M. S. Shur, D. Veksler, S. Rumyantsev, and F. Guarin, "Device loading effects on nonresonant detection of terahertz radiation by silicon MOSFETs," *Electron Lett.*, vol. 43, no. 7, pp. 422–423, Mar. 2007.
- [15] W. Stillman, D. Veksler, T. A. Elkhatib, K. Salama, F. Guarin, and M. S. Shur, "Sub-terahertz testing of silicon MOSFET," *Electron Lett.*, vol. 44, no. 22, pp. 1325–1327, Oct. 2008.
- [16] A. Gutin, S. Nahar, M. Hella, and M. Shur, "Modeling terahertz plasmonic Si FETs with SPICE," *IEEE Trans. THz Sci. Technol.*, vol. 3, no. 5, pp. 545–549, Sep. 2013.
- [17] J. S. Moon, H.-C. Seo, M. Antcliffe, S. Lin, C. McGuire, D. Le, L. O. Nyakiti, D. K. Gaskill, P. M. Campbell, K.-M. Lee, and P. Asbeck, "Graphene FET-based zero-bias RF to millimeter-wave detection," *IEEE Electron Device Lett.*, vol. 33, no. 10, pp. 1357–1359, Oct. 2012.
- [18] Z. Zhang, R. Rajavel, P. Deelman, and P. Fay, "Sub-micron area heterojunction backward diode millimeter-wave detectors with 0.18 pW/Hz<sup>1/2</sup> noise equivalent power," *IEEE Microw. Wireless Compon. Lett.*, vol. 21, no. 5, pp. 267–269, May 2011.
- [19] M. Dyakonov and M. Shur, "Detection, mixing, and frequency multiplication of terahertz radiation by two-dimensional electronic fluid," *IEEE Trans. Electron Devices*, vol. 43, no. 3, pp. 380–387, Mar. 1996.
- [20] D. M. Pozar, *Microwave and RF Design of Wireless Systems*. New York, NY, USA: Wiley, 2001.
- [21] M. I. Dyakonov, "Boundary instability of a two-dimensional electron fluid," *Semicond.*, vol. 42, no. 8, pp. 984–988, Aug. 2008.
- [22] L. F. Tiemeijer, H. M. J. Boots, R. J. Havens, A. J. Scholten, P. H. W. de Vreede, P. H. Woerlee, A. Heringa, and D. B. M. Klaasen, "A record high 150 GHz  $f_{max}$  realized at 0.18  $\mu\text{m}$  gate length in an industrial RF-CMOS technology," in *IEEE IEDM Tech. Dig.*, 2001, pp. 223–226.
- [23] U. Gogineni, "Performance limits of RF power CMOS," Ph.D. dissertation, Dept. Elect. Eng. and Compu. Sci., Mass. Inst. Technol., Cambridge, MA, USA, 2011.
- [24] C. S. Kim, J.-W. Park, H. K. Yu, and H. Cho, "Gate layout and bonding pad structure of a RF n-MOSFET for low noise performance," *IEEE Electron Device Lett.*, vol. 21, no. 12, pp. 607–609, Dec. 2000.



**Suna Kim** (M'15) received the B.S. and M.S. degrees in electrical engineering from Korea Advanced Institute of Science and Technology (KAIST), Daejeon, Korea, in 2006 and 2009, respectively, where she is currently working toward the Ph.D. degree in electrical engineering.

Her research interests include RF integrated circuit designs and further digital calibration circuit designs for wireless transceivers. Her research interests now extend to terahertz (THz) devices and circuit designs especially for THz detectors and THz imaging systems based on CMOS technology.



**Dae-Woong Park** was born in Daegu, Korea, in 1987. He received the B.S. degree from Sungkyunkwan University, Seoul, Korea, in 2013, and the M.S. degree from Korea Advanced Institute of Science and Technology (KAIST), Daejeon, Korea, in 2015, where he is currently working toward the Ph.D. degree at the Department of Electrical Engineering.

His interests include device physics and extremely high-frequency (THz) CMOS devices and circuits.



**Kyoung-Young Choi** received the B.S. degree from Kwang-Woon University, Seoul, Korea, in 2005, and the M.S. degree from Korea Advanced Institute of Science and Technology, Daejeon, Korea, in 2014.

He is currently a CMOS Image Sensor Application Engineer with System LSI, SAMSUNG, Suwon, Korea. His research interests are an optical image sensor and terahertz (THz) antenna and detectors for THz imaging systems.



**Sang-Gug Lee** (M'09) received the B.S. degree in electronic engineering from Kyungpook National University, Daegu, Korea, in 1981, and the M.S. and Ph.D. degrees in electrical engineering from the University of Florida, Gainesville, FL, USA, in 1989 and 1992, respectively.

In 1992, he joined Harris Semiconductor, Melbourne, FL, USA, where he was engaged in silicon-based RFIC designs. From 1995 to 1998, he was with Handong University, Pohang, Korea, as an Assistant Professor with the School of Computer and Electrical Engineering. From 1998 to 2009, he was with the Information and Communications University, Daejeon, Korea, and became a full Professor. Since 2009, he has been with the Department of Electrical Engineering, Korea Advanced Institute of Science and Technology (KAIST), Daejeon, Korea, as a Professor. His research interests include CMOS-based RF, analog, and mixed-mode IC designs for various radio transceivers, especially the ultra-low power applications. Lately, his research interests extend to extreme high-frequency (terahertz) circuit designs, display semiconductors, and energy-harvesting IC designs.